

17

***Ab Initio* Green's Function Calculation of Hyperfine Interactions for Shallow Defects in Semiconductors**

Uwe Gerstmann

17.1

Introduction

In semiconductor technology, besides hetero structures, shallow and deep defects are the key ingredients. The availability of mobile hole and electrons in dedicated functional regions of the material hinges on the ability to control the concentration of shallow defects. This requires a clear understanding of the physics of these important entities. In particular, the identification of defects present in a given material often is an important challenge. Here, magnetic resonance is the most sensitive experimental technique to address this essential problem. Structure identification, however, cannot be done by experiments alone. The measurements provide a set of parameters only, which have to be compared with theoretical predictions of these quantities. Only if theoretical modeling can exclude all but one structural model, then an unambiguous identification of defects has been achieved. For the modeling of the microscopic structure of the defects the electronic g -tensor and in particular their hyperfine (hf) tensors have been found to be crucial parameters as they contain detailed information on the wave function distribution on the central nucleus and the ligands, whereby the latter is often called *superhyperfine* (shf) interaction. With the development of the local spin density approximation (LSDA) of the density functional theory (DFT) [1] theoretical *ab initio* total energy methods have been introduced that describe defect structures in solids quantitatively. Nowadays many computational codes provide the possibility to calculate the hf structure of the experimental magnetic resonance spectra routinely, in most cases with the required degree of accuracy.

However, defects in semiconductors have to be divided in two groups: (1) Deep point defects seriously disturb the crystal in a small region centered at the defect site. Extremely long-ranged perturbations as *e.g.*, a Coulombic potential-tail for charged defects or strain fields are either ignored or treated as a correction. A self-consistent treatment of the deep defect is possible because it can be restricted to a small region in space, a cluster, a supercell, or to the perturbed region in a Green's function approach. (2) For shallow defects, on the other hand, the *wave function* of the defect-induced state typically extends over several hundred or even thousand unit cells and,

therefore, cannot be treated directly with *ab initio* supercell methods. Instead, the defect-induced change of the crystal potential is replaced by a model potential and the defect state is treated in an empirical one-electron approximation, the so-called effective mass approximation (EMA) [2–4]. In the simplest EMA for a substitutional donor, *e.g.*, the defect wave function is expanded into the Bloch states close to the minimum of the lowest conduction band, for which the dispersion of the band can be approximated by a parabola defining the *effective mass*. However, an empirical correction is necessary to distinct between different atomic species: the so-called *central cell correction* is introduced to describe the local part of the potential. The best EMA are then able to reproduce the binding energies of shallow acceptors and donors. The empirical character of the EMA, however, prevents a prediction of the hf and shf parameters, decisive for an identification of the atomic structures. As a result, the wealth of information contained in the (s)hf interaction data for shallow dopants, the technologically most important class of defects, is completely obscured.

In this article, we show that within a Green's function approach the *central cell* correction as the empirical part of the EMA can be substituted by an *ab initio* calculation of this quantity. By this, a prediction of hf splittings becomes possible, within an accuracy comparable with that in case of deep defects. This article is organized as follows: first, we discuss the microscopic origin of the hf structure showing that DFT is perfectly suited to allow an accurate computation. Then a Green's function method is applied onto deep defects, whereby lattice relaxation is taken into account if calculating the hf splittings. Thereafter, based on a short review of the EMA and its empirical extensions, we present how the *ab initio* calculated local part of the potential is embedded via Green's functions into an EMA-like background. Finally, the approach is applied onto shallow donors in silicon and silicon carbide (SiC).

17.2

From DFT to Hyperfine Interactions

17.2.1

DFT and Local Spin Density Approximation

Our main target is the calculation of the hf splittings within a many-body problem given by the nuclei and the density of the surrounding electrons. In a first step we get rid of the nuclear degrees of freedom using the Born–Oppenheimer approximation. According the theorem by Hohenberg and Kohn [5] the (non-degenerate) ground state energy of the remaining many-electron system is a unique functional $E[n]$ of this electron density which, thus, provides the starting point of DFT. From a general many-electron wave function Ψ it can be obtained via

$$n(\mathbf{r}) = \langle \Psi | \sum_{i=1}^{N_e} \delta(\mathbf{r} - \mathbf{r}_i) | \Psi \rangle. \quad (17.1)$$

The theory can easily be extended to include the spin polarization: Following von Barth and Hedin [6], we assume that an external magnetic field defines the direction

of spin quantization with $\sigma = \uparrow, \downarrow$. The ground state energy is then a unique functional $E[n_\sigma]$ of the spin-polarized electron densities (the *spin densities*) or alternatively a unique functional $E[n, m]$ of the electron density

$$n(\mathbf{r}) = n_\uparrow(\mathbf{r}) + n_\downarrow(\mathbf{r}) \quad (17.2)$$

and the magnetization density

$$m(\mathbf{r}) = n_\uparrow(\mathbf{r}) - n_\downarrow(\mathbf{r}). \quad (17.3)$$

Kohn and Sham [7] have shown that the density $n(\mathbf{r})$ for interacting fermions can be mapped onto the density for a system of non-interacting particles that are subject to some extra energy, the exchange-correlation energy $E_{xc}[n, m]$. For non-interacting particles we know that the density $n_\sigma(\mathbf{r})$ can be expanded into the sum of squared single-particle orbitals $\phi_{l,\sigma}(\mathbf{r})$

$$n_\sigma(\mathbf{r}) = \sum_{l=1}^{N_\sigma} |\phi_{l,\sigma}(\mathbf{r})|^2. \quad (17.4)$$

For practical use these orbitals $\phi_{l,\sigma}(\mathbf{r})$ are the solution of coupled single-particle equations (the *Kohn–Sham equations*), whereby the electrons move in a spin-polarized effective potential

$$V_{\text{eff},\sigma}(\mathbf{r}) = V_{\text{ext}}(\mathbf{r}) + e^2 \int \frac{n(\mathbf{r}')}{|\mathbf{r} - \mathbf{r}'|} d^3\mathbf{r}' + V_{xc,\sigma}^{\text{DFT}}[n, m], \quad (17.5)$$

given by the external potential V_{ext} , the Coulomb-potential of the electrons, completed by the exchange-correlation potential $V_{xc,\sigma}^{\text{DFT}}[n, m]$ that includes the many-particle contributions and that depends on the spin direction σ , on the electron density $n(\mathbf{r})$, and also on the magnetization density $m(\mathbf{r})$. The exact shape of this non-local exchange-correlation potential

$$V_{xc,\sigma}^{\text{DFT}}[n, m] = \frac{\delta E_{xc}^{\text{DFT}}[n, m]}{\delta n_\sigma(\mathbf{r})} \quad (17.6)$$

is unknown. For practical applications, however, there are useful parametrization schemes which approximate the exchange-correlation potential [8, 9] calculated for a homogeneous spin-polarized electron gas. The resulting $V_{xc,\sigma}^{\text{LSDA}}[n, m] = V_{xc,\sigma}^{\text{LSDA}}(n(\mathbf{r}), m(\mathbf{r}))$ depends only locally on the spin densities. This local density approximation (LDA) of DFT has proven to yield approximate results with an accuracy going far beyond the early expectations [1]. The perhaps most crucial shortcoming of the LSDA can be found in connection with the fundamental band gap of semiconductors as the gap of the single-particle energies turn out to be too small by about a factor of two. The reason for this is a discontinuity upon a change of the particle number that would be present in the exact exchange-correlation functional [10, 11], but is absent in the LSDA [12]. We will come back to this point later.

17.2.2

Scalar Relativistic Hyperfine Interactions

Within the LSDA it is also possible to calculate the hf interaction of the magnetic moments of the electrons with those of the nuclei. The influence of an external magnetic field B_0 (in the range of some 100 mT) typically leads to level splittings in the $10^{-12} \dots 10^{-2}$ eV range. The smallness of the magnetic field-induced level splittings *simplifies* the computation considerably, and the influence of an external magnetic field can be described by perturbation theory.

Although there exist a non-relativistic derivation for the isotropic contact interaction (Fermi [13]), Breit has shown that the origin of the hf splitting can be only described correctly in a relativistic treatment [14]. The static magnetic field $B(\mathbf{r}) = \nabla \times \mathbf{A}(\mathbf{r})$ caused by the magnetic moment $\boldsymbol{\mu}_I = g_N \mu_N \mathbf{I}$ of a nucleus with gyromagnetic ratio g_N located at the origin is obtained using the vector potential

$$\mathbf{A}(\mathbf{r}) = \nabla \times \left(\frac{\boldsymbol{\mu}_I}{r} \right). \quad (17.7)$$

By replacing the momentum operator \mathbf{p} in Dirac's equation

$$(c\boldsymbol{\alpha} \cdot \mathbf{p} + \beta mc^2 + V_{\text{eff}} - E_{\text{rel}})|\Psi\rangle = 0 \quad (17.8)$$

by the canonical momentum $\boldsymbol{\pi} = \mathbf{p} - e/c\mathbf{A}$ the expectation value of the hf interaction is, thus, given in first order perturbation theory by

$$E_{\text{HF}} = -e\langle\Psi|\boldsymbol{\alpha} \cdot \mathbf{A}(\mathbf{r})|\Psi\rangle. \quad (17.9)$$

Here, $\boldsymbol{\alpha}$ is a vector of 4×4 matrices constructed from the 2×2 Pauli spin matrices σ_x , σ_y , and σ_z , respectively, whereby $|\Psi\rangle = \begin{pmatrix} \Phi_L \\ \Phi_S \end{pmatrix}$ is given by the Dirac spinor, decomposing into the two-component Pauli spinors Φ_L and Φ_S . For light atoms, Φ_L is the dominant, large component whereas Φ_S turns out to be small. This leads to

$$E_{\text{HF}} = -e(\langle\Phi_L|\boldsymbol{\sigma} \cdot \mathbf{A}(\mathbf{r})|\Phi_S\rangle + \langle\Phi_S|\boldsymbol{\sigma} \cdot \mathbf{A}(\mathbf{r})|\Phi_L\rangle). \quad (17.10)$$

Thus, E_{HF} is a genuine relativistic term that couples large and small components of Dirac's equation. The small component Φ_S can be expressed in terms of the large component Φ_L as

$$\Phi_S = \frac{c\boldsymbol{\sigma} \cdot \mathbf{p}}{2mc^2 + E - V_{\text{eff}}(\mathbf{r})}\Phi_L = \frac{S(\mathbf{r})}{2mc^2}(\boldsymbol{\sigma} \cdot \mathbf{p})\Phi_L, \quad (17.11)$$

whereby $S(r)$ is the inverse relativistic mass correction. By this, the hf splitting

$$E_{\text{HF}} = E_{\text{contact}} + E_{\text{orb}} + E_{\text{dip}}, \quad (17.12)$$

is the sum over the following expectation values containing the large component only [15]:

$$E_{\text{contact}} = -\frac{8\pi}{3} \mu_B \langle \Phi_L | S(\mathbf{r}) \mu_I \cdot \sigma \delta(\mathbf{r}) | \Phi_L \rangle \\ + \langle \Phi_L | \frac{1}{r^4} \frac{\partial S}{\partial r} [\mu_I \cdot \sigma r^2 - (\mu_I \cdot \mathbf{r})(\sigma \cdot \mathbf{r})] | \Phi_L \rangle, \quad (17.13)$$

$$E_{\text{orb}} = -\frac{e}{mc} \mu_I \cdot \langle \Phi_L | \frac{\mathbf{L}}{r^3} | \Phi_L \rangle, \quad (17.14)$$

$$E_{\text{dip}} = \mu_B \langle \Phi_L | \frac{1}{r^5} [\sigma \cdot \mu_I r^2 - 3(\sigma \cdot \mathbf{r})(\mu_I \cdot \mathbf{r})] | \Phi_L \rangle. \quad (17.15)$$

In the non-relativistic limit, since $S(\mathbf{r}) \rightarrow 1$, only the first term in Eq. (17.13) contributes to the isotropic contact term E_{contact} . By this, we obtain the results of the classical theory given by Fermi [13], that only the probability amplitude at the nucleus contributes. In the relativistic case, however, this first term does not contribute at all. It is the second term in Eq. (17.13) which is the relativistic analog to the contact interaction. For a pure Coulomb-potential around a given nucleus we obtain

$$V_{\text{eff}}(r) \approx \frac{-Ze^2}{r}, \quad (17.16)$$

and the derivative $\partial S(r)/\partial r$ is similar to a broadened δ -function

$$\delta_{\text{Th}}(\mathbf{r}) = \frac{1}{4\pi r^2} \frac{\partial S}{\partial r} = \frac{1}{4\pi r^2} \frac{r_{\text{Th}}/2}{\left[\left(1 + \frac{E}{2mc^2}\right) r + \frac{r_{\text{Th}}}{2} \right]^2}. \quad (17.17)$$

In other words, the magnetization density of the electron in the relativistic theory is not simply evaluated at the origin, where it would be divergent for s -electrons, but is averaged over a sphere of radius

$$r_{\text{Th}} = \frac{Ze^2}{mc^2}, \quad (17.18)$$

which is the Thomson radius, about ten times the nuclear radius. As a result, the divergence of the s -electrons presents no problem. Also if we approximate the nuclear potential by that of a charged volume rather than that of a point charge [16], the divergence already disappears. However, it is important to note, that we would obtain divergent contact terms mixing the approximations, *e.g.*, using (scalar)¹⁾ relativistic orbitals in a non-relativistic formula.

If the ground state of the defect is a single determinantal orbital singlet state with total spin S , we have the simple case where the orbital angular momentum

1) In the scalar relativistic treatment Φ_L is calculated solving Dirac's equation but thereby ignoring spin-orbit interactions. This leaves the electron spin as a "good" quantum number. Already in a scalar relativistic treatment, s -like wave functions diverge at the nuclear site (if the nucleus is taken to be a point charge).

is “quenched” [17]. The orbital state transforms like an angular momentum eigenfunction with quantum number $l = 0$. Hence, the expectation value of the angular momentum operator vanish, and there are no orbital contributions E_{orb} to the hf interactions. Writing the N -particle wave function $|\Phi_L\rangle = |S, M_S\rangle$ as a single Slater determinantal in real space representation, the hf interaction is then fully described by the matrix elements $\langle S, M_S | \mathcal{H}_{\text{HF}} | S, M'_S \rangle$ with respect to the spin Hamiltonian

$$\mathcal{H}_{\text{HF}} = \sum_k \{a_k \mathbf{S} \cdot \mathbf{I}_k + \mathbf{S} \cdot \mathbf{B}_k \cdot \mathbf{I}_k\}. \quad (17.19)$$

It is important to note that the matrix elements ($\mathbf{r}_k = \mathbf{r} - \mathbf{R}_k$)

$$a_k = \frac{1}{2S} \frac{8\pi}{3} \gamma_k \int m(\mathbf{r}) \delta_{\text{TH}}(\mathbf{r}_k) d^3\mathbf{r}, \quad (17.20)$$

$$\mathbf{B}_k = \frac{1}{2S} \gamma_k \int m(\mathbf{r}) \frac{3\mathbf{r}_k \otimes \mathbf{r}_k - r_k^2 \mathbf{1}}{r_k^5} d^3\mathbf{r}, \quad (17.21)$$

can be expressed as a sum over *single-particle* matrix elements with respect to the magnetization density without the need to *construct many-body* wave functions first. We have simply to insert the magnetization densities obtained from the self-consistent LSDA calculation and obtain the hf interactions with the central nucleus as well as with the ligands (ligand hf interactions or shf interactions). Since each of the \mathbf{B}_k is traceless, its diagonal elements can be parametrized by two parameters b_k and b'_k , describing the axial and non-axial part of the anisotropy.

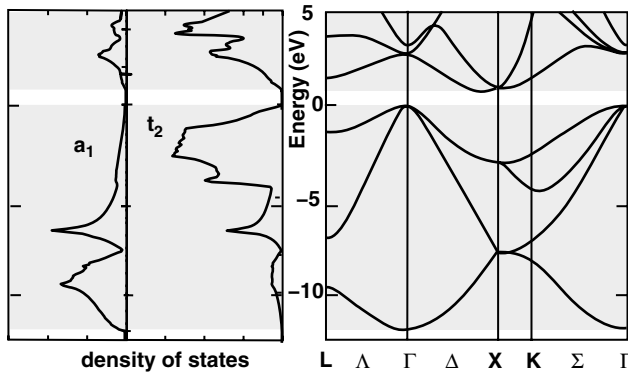


Figure 17.1 The density of states (DOS) distribution for the silicon crystal broken up into states transforming according to a_1 (left) and to t_2 (right), is compared with the energy bands plotted along the high-symmetry directions.

17.3

Modeling Defect Structures

17.3.1

The Green's Function Method and Dyson's Equation

By introducing a point defect into the otherwise perfect crystal we break the translational symmetry, and the periodicity of the ideal crystal is lost. Nevertheless, the method most frequently used for the computation of point defects in solids is the supercell method: instead of an isolated system with a single point defect one considers a three-dimensional lattice of clusters, each with a single point defect. This crystal can be treated theoretically by the known methods of energy band theory, however, with the cluster as the “supercell” unit cell.

The Green's function method [18–20] embeds a single defect into an otherwise perfect crystal (cf. Figure 17.2). For this system the effective potential V_{eff} is split into the effective potential V_{eff}^0 of the undisturbed crystal plus some short-ranged impurity-related potential ΔV

$$V_{\text{eff}} = V_{\text{eff}}^0 + \Delta V. \quad (17.22)$$

ΔV can be quite large at the defect site but will decay rapidly with the distance from the defect center. The Green's function, G_0 , for a perfect crystal characterized by the Hamiltonian H_0 is defined as [21]

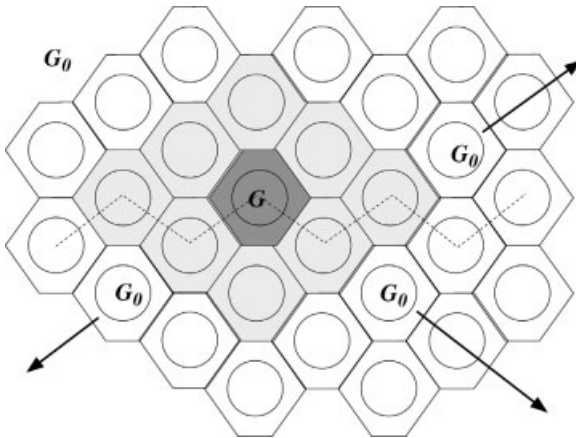


Figure 17.2 (online color at: www.pss-b.com) Dyson's equation: A perturbation ΔV is embedded into a reference system characterized by the “unperturbed” Green's function G_0 . Within the perturbed region

(colored) the Green's function G of the perturbed system is determined via Eq. (17.29): $G = (1 - G_0 \Delta V)^{-1} G_0$. Outside this region, G remains unchanged and matches G_0 .

$$G_0(E) = \lim_{\varepsilon \rightarrow 0^+} \frac{1}{E - i\varepsilon - H_0}. \quad (17.23)$$

A small imaginary part added to the energy prevents a singularity for $E = E_{n,\mathbf{k}}$ i.e., within the valence and conduction bands (cf. Figure 17.1). G_0 can be expressed in terms of Bloch functions $|\varphi_{n,\mathbf{k},\sigma}\rangle$ for the spin state σ , which solve the Kohn–Sham equations for the perfect crystal:

$$G_0(E) = \lim_{\varepsilon \rightarrow 0^+} \sum_{n,\mathbf{k},\sigma} \frac{|\varphi_{n,\mathbf{k},\sigma}\rangle \langle \varphi_{n,\mathbf{k},\sigma}|}{E - i\varepsilon - E_{n,\mathbf{k},\sigma}}. \quad (17.24)$$

The sum in Eq. (17.24) includes all states $\{n, \mathbf{k}, \sigma\}$, not just the occupied states. *Vice versa*, the Green's function G for a given system includes all electronic ground state properties of this system. The full information of the density of states distribution (DOS)

$$D(E) = \frac{1}{\pi} \mathcal{I}m \operatorname{Tr}\{G(E)\} \quad (17.25)$$

and most important the (spin-polarized) electron densities are obtained by summing up the occupied bands only

$$n_\sigma(\mathbf{r}) = \frac{1}{\pi} \mathcal{I}m \left\{ \int_{\text{occ.}} G^\sigma(E, \mathbf{r}, \mathbf{r}) dE \right\}. \quad (17.26)$$

For a crystal containing a deep defect, the Green's function G corresponding to the full Hamiltonian H reads

$$G(E) = \lim_{\varepsilon \rightarrow 0^+} \frac{1}{E - i\varepsilon - H}, \quad (17.27)$$

where the Hamiltonian now contains the full effective potential V_{eff} . The Green's function G is related to G_0 by a Dyson equation

$$G = G_0 + G_0 \Delta V G, \quad (17.28)$$

which can be solved iteratively

$$G = (1 - G_0 \Delta V)^{-1} G_0. \quad (17.29)$$

The solution of Eq. (17.29) is possible if we have to invert $(1 - G_0 \Delta V)$ only in the vicinity of the defect, the “perturbed region”, where ΔV is non-negligible. In contrast, the Green's functions G_0 and G extend outside this perturbed region. Despite the localized shape of the “perturbation” ΔV , the approach via Dyson's equation is very flexible. Nowadays, it is a standard tool to describe transport properties in microscopic nanostructures [22], whereby ΔV is determined by the conductance electrons.

One result of a self-consistent calculation of Dyson's equation for a defect is the electron density $n(\mathbf{r})$. It can, of course, also be decomposed into contributions from different spin directions $n_\sigma(\mathbf{r})$. For the hf interactions we will need the magnetization density

$$m(\mathbf{r}) = \frac{1}{\pi} \mathcal{I}m \left\{ \int_{\text{occ.}} [G^\dagger(E, \mathbf{r}, \mathbf{r}) - G^\dagger(E, \mathbf{r}, \mathbf{r})] dE \right\}. \quad (17.30)$$

We have already noted in Section 17.2.1 that in fully converged LDA calculations the fundamental band gap turns out to be too small. For silicon, this difference is about 0.5 eV and for wide band gap semiconductors like GaAs, GaN, or SiC, the error is in the range of 1 eV or even larger. In some cases, defect-induced gap states, which should be located in the upper part of the gap, are calculated to be resonances in the conduction band. Also if this worst case scenario is not given, the hf interaction can be affected [23]. The Green's function method provides a way to circumvent this problem by a rigid shift of the crystalline conduction bands by some amount ΔE_{shift} with respect to the valence bands, before calculating G_0 . This formalism, called scissor operator $\text{Sc}\{E\} = E + \Delta E_{\text{shift}}$, was introduced by Baraff and Schlüter [24]. Hence, by substituting Eq. (17.24) by

$$G_0(E) = \lim_{\varepsilon \rightarrow 0^+} \sum_{n, \mathbf{k}, \sigma} \frac{|\Phi_{n, \mathbf{k}, \sigma}\rangle \langle \Phi_{n, \mathbf{k}, \sigma}|}{E - i\varepsilon - \text{Sc}\{E_{n, \mathbf{k}, \sigma}\}}, \quad (17.31)$$

we are able to adjust the fundamental gap to a given experimental value. It is important to note here that this has to be done only once, namely if calculating the Green's function of the ideal crystal. Afterwards, since the Green's function approach is applied in real space without the need of periodic images, the band edges are retained, and each one-particle level is corrected automatically in a self-consistent way.

17.3.2

The Linear Muffin-Tin Orbital (LMTO) Method

For a periodic system like a crystal, one might consider a plane wave expansion to be the simplest computational method. And indeed, most supercell calculations use the pseudopotential method for which the inclusion of short-ranged lattice relaxations is relatively straightforward. Since by construction the pseudo-wave functions do not include the rapid oscillations in the core region, the resulting spin pseudo-wave densities are not directly applicable for the computation of hf interaction matrix elements, determined in the vicinity of the nuclei. Van de Walle and Blöchl [25] used a projector formalism to reconstruct the original wave function from the pseudo-functions. Alternatively, in the muffin-tin methods, V_{eff} is assumed to be spherically symmetrical within atomic spheres around R_j ,

$$V(\mathbf{r} - \mathbf{R}_j) = \begin{cases} V(|\mathbf{r} - \mathbf{R}_j|) & \text{if } |\mathbf{r} - \mathbf{R}_j| \leq s_j \\ \text{const.} & \text{else,} \end{cases} \quad (17.32)$$

and the Kohn–Sham orbitals are expanded into spherical harmonics times a radial solution. Different muffin-tin methods are in use which differ in the technical procedure used to construct a regular Bloch wave from the partial wave solutions obtained within the atomic spheres: the Korringa–Kohn–Rostocker (KKR) method

[26, 27], the linear muffin-tin orbital (LMTO) method [28, 29], and the linearized augmented plane wave (LAPW) method [30]. Compared with the pseudopotential method the muffin-tin methods have the advantage that the correct electron and magnetization density in the nuclear region can be directly and very accurately obtained, which is decisive for the hf interaction. All muffin-tin methods, however, share the disadvantage that they are technically difficult and, due to the use of atomic spheres, less flexible with respect to larger lattice relaxations, although there are full-potential versions of all the muffin-tin methods, FP-KKR [31], FP-LMTO [32], and F-LAPW [33].

In this work, we use the LMTO-ASA method since it provides perhaps the easiest and straightforward way to realize the Green's function method via a muffin-tin approach [20]. In the atomic spheres approximation (ASA) the sphere radii for the integrals are chosen such that the unit cell volume equals to the sum of the ASA sphere volumes. In this approximation, the ASA spheres overlap slightly and the contribution of the neglected regions are assumed to be cancelled by the double-counted overlap. For open structures like semiconductors, additional “empty” spheres centered around the highly symmetrical interstitial sites of the lattice have to be inserted in order to optimize the volume-filling. We have extended the LMTO-ASA Green's function approach to include moderate lattice relaxations. For the resulting distorted structures the concept of space-filling ASA spheres is no more straightforward. Here, the concept of a Voronoi tessellation is very helpful (*cf.* Figure 17.3), whereby the decomposition of a metric space is determined by distances to a discrete set of points, the center of the Voronoi cells (either given by a nucleus or the center of an empty cell) [34]. The concept can be easily extended to hetero-atomic structures using a weighted decomposition. Here, we use the so-called Bragg–Slater radii [35], whereby the ASA condition of space-filling spheres can be easily fulfilled by constructing an ASA sphere S_j with radius s_j to each Voronoi cell Z_j :

$$V(S_j) = V(Z_j). \quad (17.33)$$

Using in this way extended ASA approximation, we solve Dyson's equation in LMTO matrix representation [20]

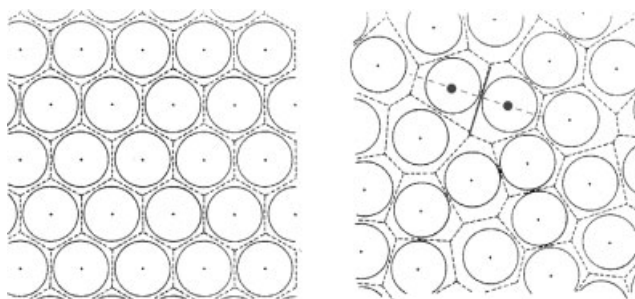


Figure 17.3 (online color at: www.pss-b.com) Wigner–Seitz cells of a two-dimensional regular structure (left) and in comparison a disordered structure divided into Voronoi cells (right). Possible non-overlapping muffin-tin radii are also given.

$$\{1 + g^0(E)[\Delta P(E) - \Delta S]\}g(E) = g^0(E), \quad (17.34)$$

within a “perturbed region” large enough to allow a proper description of ΔS and ΔP . Here, $\Delta P = P - P^0$ is the localized, diagonal perturbation of the so-called potential function [20] describing the electronic structure of the investigated atomic structure, and ensuring that the partial waves from the muffin-tin spheres fulfill the correct bounding conditions. $\Delta S = S_{R'L',RL} - S_{R_0'L',R_0L}$ is the relaxation-induced change of the LMTO-ASA structure constants

$$S_{R'L',RL} = (-1)^{l+1} 8\pi \sum_{l''} \frac{l!l''!(2l')!}{(2l)!(2l')!l''!} \left(\frac{a}{d_{RR'}}\right)^{l+l'+1} \sum_{m''} C_{LL'L'} Y_{L''}(\hat{d}_{RR'}), \quad (17.35)$$

whereby $C_{LL'L''} := \int_{\Omega} Y_L(\hat{r}) Y_{L''}^*(\hat{r}) Y_{L'}(\hat{r}) d\Omega$ and $Y_L(\hat{r})$ as spherical harmonics with $L = (l, m)$. The calculation of the rather extended matrix ΔS is more elaborate: the long-ranged tails of the matrix elements are split up and treated by generalized Ewald sums [36], whereas the short-ranged contribution are calculated in a next-nearest neighbor approximation.

In the general case, the atomic position $\{\mathbf{R}\}$ of the relaxed structure can be taken from pseudopotential calculations. The electronic structure to the relaxed structures can then be calculated via Eq. (17.34), including the (s)hf parameters of paramagnetic states. We will see, however, that in some cases with rather moderate relaxation, the extended LMTO-ASA GF approach is also able to predict at least the nearest neighbor relaxation.

17.3.3

The Size of The Perturbed Region

Using a Green’s function method, the spin densities arising from the defect states are not completely contained in the rather limited volume of the perturbed region. Surprisingly, this does not cause a problem as will be shown in the following, taking the isolated As_{Ga}^+ antisite in GaAs as a reference system (Table 17.1 where also well established experimental data is available):

The gap state, that mainly gives rise to the magnetization density (See Figure 17.4) and, thus, to the hf interaction of the paramagnetic As_{Ga}^+ charge state, transforms according to the a_1 irreducible representation of the group T_d . For the neutral and the two-fold positive, diamagnetic charge states, this state is unoccupied. The total energies, E_{tot} , and the single particle eigenvalues of this gap state, $E(a_1)$, also shown in Table 17.1 seem to depend on N_{atoms} in a rather unsystematic manner. However, the variation of E_{tot} for the E^{2+} and E^0 charge states is practically identical with that for E^+ , and therefore, the charge transfer energies are essentially independent of N_{atoms} .

In Table 17.1 we also show the convergence of the corresponding hf interactions, calculated using perturbed regions of different sizes. The magnetization density is mainly concentrated on the central antisite atom, where it gives rise to the largest nearly isotropic hf splitting, and on its four nearest neighbors, where it is predom-

Table 17.1 The influence of the size of the perturbed region on the total energy, E_{tot} , the gap state energy $E(a_1)$, the magnetic moment of the gap state μ_{gap} and the total magnetic moment μ_{pert} within the perturbed region, as well as the hf interactions (MHz) (upper line for a , lower line for b) for the 3% outward relaxed

isolated As_{Ga}^+ antisite in GaAs. Beside the hf values for the central As_{Ga}^+ nucleus, the shf splittings due to several neighbor shells of the crystal host are also given. N_{atoms} is the number of atomic ASA spheres in the perturbed region. Experimental data taken from Refs. [37, 38].

N_{atoms}	E_{tot}	$E(a_1)$	μ_{gap}	μ_{pert}	As_{Ga}^+ (0,0,0)	As (1,1,1)	Ga (2,2,0)	As (1,1,3)	As (3,3,1)
1	−107.83	1.478	0.097	0.113	2811.				
5	−107.47	0.988	0.469	0.499	2778.	187.7			
						46.1			
11	−108.09	1.080	0.572	0.598	2846.	175.3	8.8		
						45.8	1.5		
23	−108.04	1.063	0.614	0.638	2839.	175.8	7.4	0.3	
						45.7	1.5	−0.2	
47	−107.82	0.995	0.817	0.840	2879.	173.2	3.9	0.1	22.3
						46.6	1.4	−1.9	4.2
exp.					2650.	169.3	−	−	21.5
						53.2	−	−	2.2

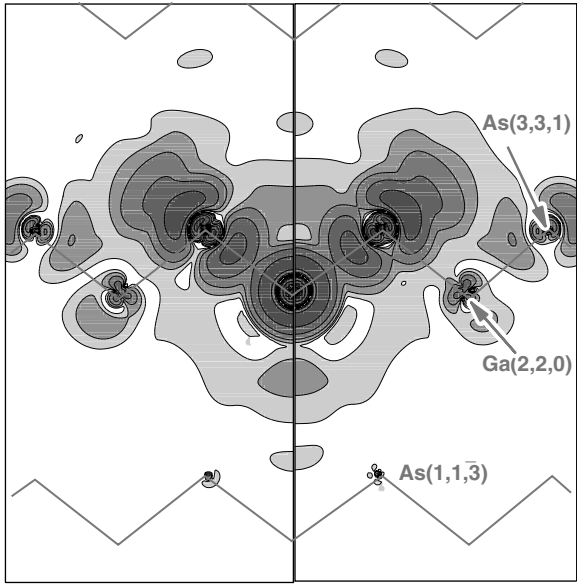


Figure 17.4 (online color at: www.pss-b.com) Contour plot of the magnetization density for the isolated As_{Ga}^+ antisite in a (110) plane in GaAs (taken from Ref. [44]). The left panel shows the contribution of the gap state, the right

part gives the total magnetization density. The Ga (As) lattice sites are at the lower (upper) side of the zig-zag chain of nearest neighbor bonds, respectively.

inantly *p*-like. The smallest conceivable perturbed region consisting of the defect ASA sphere alone contains about 10% of the magnetic moment of the defect. Yet, we obtain a central contact hf interaction at the As_{Ga} antisite nucleus which is only 2% smaller than the value obtained for the largest perturbed region with 47 atoms. It is obvious and quite impressive that via the Green's function approach the defect is really embedded in an infinite background. Even if we do not present the data explicitly, the reader should believe that this procedure also works in the case of a vacancy: only an empty sphere is then necessary to obtain at least rough estimates. From Table 17.1 we see that for different sizes of the perturbed region the hf interactions with the nuclei at the “surface” of the perturbed region is slightly overestimated. With a further increase of N_{atoms} the corresponding values are reduced to better values. For the contact hf interactions of the more distant Ga (2,2,0) and As(1,1, 3) ligands the convergence apparently is quite poor, but here the magnetic moments for the ligand ASA shells are extremely small. The value of 4 MHz for the contact interaction with a [69] Ga nucleus corresponds to 2×10^{-4} of a single *s*-like spin only.

17.3.4

Lattice Relaxation: The As_{Ga} -Family

Experimentally well understood, the isolated As_{Ga} antisite is only one member of the technologically very important As_{Ga} -family: At least four different As_{Ga} -related defects with almost identical hf structure have been detected by magnetic resonance [37–39]. Their thermal stability is quite puzzling: the well established isolated As_{Ga} defect is obtained by low-temperature electron irradiation of semi-insulating GaAs and disappears at room temperature [40], when in electron-irradiated material the so-far unidentified $\text{As}_{\text{Ga}}\text{-X}_1$ defect is observed. At $T = 520$ K the $\text{As}_{\text{Ga}}\text{-X}_1$ defect disappears and the so-called EL2 becomes dominant. The latter defect is quite stable. It is the dominant defect in semi-insulating GaAs [41, 42] where it determines the position of the Fermi level. The EL2 can be eliminated by a rapid quench from 1100 °C [43] and is recovered by annealing the sample above 750 °C. Its paramagnetic properties strongly suggest the EL2 to be a nearly tetrahedral defect. If the EL2 is not the isolated antisite it should be, thus, at least some pair or complex with some other partners. However, the exact microscopic structure of the EL2 defect is still controversial (for a review, see Refs. [39, 44]).

Another interesting aspect of the members of the family of As_{Ga} -related defects is their metastability. Theoretical *ab initio* calculations [45–47] have shown that a lattice relaxation around the As_{Ga} antisite atom is responsible for the defect metastability. We have, thus, investigated the influence of the lattice relaxation onto the hf interaction (See Table 17.1 for the largest perturbed region). For the isolated tetrahedral point defects a symmetry-conserving relaxation of the nearest neighbors was included to determine the lattice relaxation from the minimum of the total energy. For the neutral isolated As_{Ga}^0 point defect we find a minimum of the total energy if the distance to the nearest neighbors is increased by 4.7% with respect to the bond-length in the unperturbed crystal. The energy gained by this relaxation is

0.32 eV. A very similar relaxation (4.0%, 0.33 eV energy gain) was reported by Dabrowski and Scheffler [45] for a 54-atom supercell calculation. For the defect in the singly positive, paramagnetic charge state the relaxation reduces to 3% (1.4% for the double positive charge state). For the relaxed defects the calculated charge transition energies are $E^{2+/+} = E_v + 0.98$ eV and $E^{+/0} = E_v + 1.18$ eV, if the band gap is adjusted to the experimental value by the Scissor operator, somewhat smaller than the results (1.25 and 1.5 eV, respectively) obtained by Baraff and Schlüter [48] and by Delerue [49]. Without such an adjustment of the gap, the charge transition energies would be $E_v + 0.37$ eV and $E_v + 0.55$ eV, respectively.

Figure 17.5 shows the calculated total energy for the isolated As_{Ga}^+ defect as a function of the nearest neighbor distance d for a relaxation that does not alter the tetrahedral defect symmetry. Also shown is the dependence of the hf interactions with the antisite nucleus and of the shf interactions with the nearest neighbors. As is the case for all deep donor states, the hf interaction with the donor nucleus is quite sensitively dependent on the nearest neighbor distance. In our case, the moderate 3% outward relaxation obtained for the minimum of the total energy leads to a 7% decrease of the hf interaction with the central nucleus (the same relaxation leads to a 9% decrease of the isotropic shf interaction and a 5% increase of the anisotropic shf interaction with the nearest neighbor nuclei).

Similar to the case of elemental semiconductors [50], the magnetization density is the subject of strong oscillations (See also Table 17.1): The shf splittings are rather small at the (2,2,0) and (1, 1, $\bar{3}$) neighbors, but again much larger at the more distant (3,3,1) neighbor, the fifth shell of neighbors. In particular, there are no larger interactions with the Ga nuclei, in agreement with the fact that these have not been

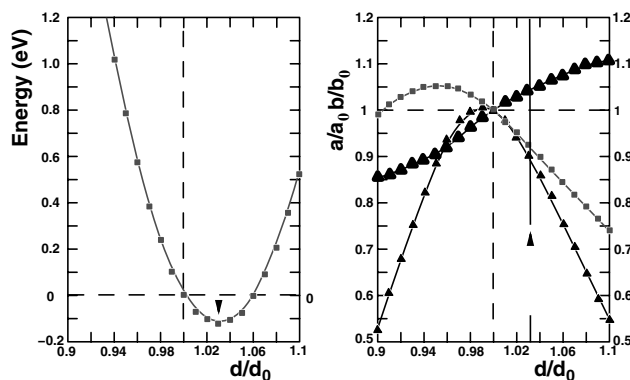


Figure 17.5 (online color at: www.pss-b.com) Calculated total energy for the As_{Ga}^+ antisite as a function of the nearest neighbor distance d (left). d_0 is the nearest neighbor distance for the unrelaxed GaAs crystal. The right panel shows the relative change of the hf interactions upon

relaxation normalized to its respective unrelaxed values a_0 and b_0 : Contact interaction with the antisite nucleus (square) and contact (full triangle) and dipolar (open triangle) interactions with the nearest neighbor nucleus.

detected by (optical detected) electron nuclear double resonance (OD)ENDOR. A detailed comparison with experimental data [37] shows a close agreement already for the interactions that had been calculated without taking into account a lattice relaxation. Nevertheless, the agreement is substantially improved if the lattice relaxation is included.

Since the hf interactions both with the central As nucleus and with the first shell of As ligands are strikingly similar for all members of the As_{Ga} family, it can be excluded that the experimentally observed paramagnetic states of any member of the As_{Ga} family are subject to a major lattice relaxation of the As_{Ga} nucleus. In Ref. [44] it has been furthermore shown that for the technologically important EL2 defect the $\text{As}_{\text{Ga}}\text{--As}_i$ model can be excluded based on this argument and high-field OD(ENDOR) experiments [51]. Since a slight but definite deviation from tetrahedral symmetry is observed in these experiments, it appears that the *thermally most stable* defect in the As_{Ga} family is some defect aggregate. This at first view paradox observation has been proposed as the most likely solution, in which near room temperature the EL2 transforms to an isolated tetrahedral defect and that the deviations from tetrahedral symmetry observed experimentally are caused by the pairing with some other mobile defect, e.g., *shallow* acceptors or donors, which occur while cooling the sample.

17.4

Shallow Defects: Effective Mass Approximation (EMA) and Beyond

In the last section we have seen that shallow dopants, acceptors as well as donors can form complexes with intrinsic defects. In these complexes, the dopant levels appear in ionized form, so that the resulting complex form again a deep defect. Also the ionized charge state of an isolated donor is a deep defect, and the defect-induced change of the DOS is well localized. In the neutral charge state of the defect, however, the additional electron is rather extended. Only weakly bound, the donor electron provokes a hydrogen-like series of bound states with binding energies small compared to the fundamental band gap and with an effective Bohr radius that may exceed 100 Å. Whereas now a days supercell calculations of up to 1000 atoms nicely describe the ionization energies, the quantitative description of the spatial distribution of the wave function still remains a challenge. We will illustrate this problem taking conduction electrons in 4H-SiC as an example: Here, the delocalization of the electron wave function can be characterized by an effective Bohr radius of about 13 Å [52]. As a consequence, only 30% of the donor electron are found in a region containing 750 atoms around the donor atom (Figure 17.6). This is also demonstrated by recent 576-atom supercell calculations [53] where in comparison with experiment the localization of the donor wave function at a central P nucleus and the four neighboring ligands is overestimated by a factor of three (2.1% instead of 0.8%). In other words, the usual *ab initio* methods still cannot be used straightforward to treat the shf structure of these strongly delocalized defect states. Instead, we fall back on the *empirical* EMA as a standard tool to describe the *wave function* of shallow defects.

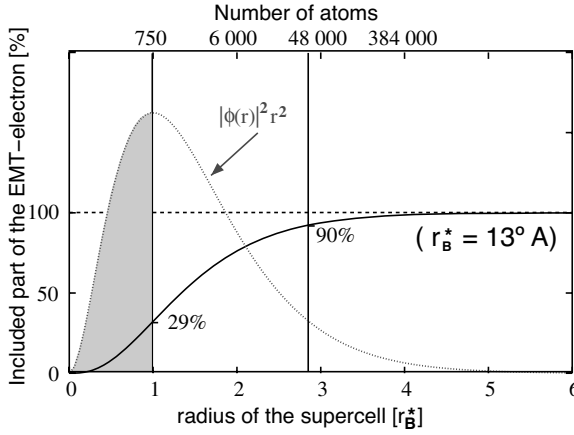


Figure 17.6 (online color at: www.pss-b.com) Delocalization of EMA-like donors: The radial probability distribution $|\Phi(r)|^2 r^2$ becomes maximum at the effective Bohr radius r_B^* . But only 29% of the electron are found in a sphere of radius r_B^* (solid curve). For 4H-SiC with

$r_B^* = 13 \text{ \AA}$ [52] e.g., huge supercells with more than 40 000 atoms would be necessary to reduce the artificial overlap of the periodic images of the wave functions to a more or less acceptable value below 10%.

The EMA “predicts” ionization energies and in addition the hydrogen-like series of bound states that agree sufficiently well with experimental data (for a review, see the classical article by Kohn [4] or the more recent article by Ramdas and Rodriguez [54]).

The comparison with experimental EPR data, however, shows the EMA results for the shf interactions to be at most qualitatively correct. In the following, this apparent failure of the EMA is discussed in comparison with results of an empirical pseudopotential calculation that provides accurate donor binding energies and corrected wave functions. Finally, we show that a Green’s function based method allows an *ab initio* description of the magnetization density of shallow defects, including the resulting hf and shf splittings.

17.4.1

The EMA Formalism

The problem of a shallow defect can be divided into two parts: $D^0 = D^+ + e^-$. Providing a deep defect, the ionized donor D^+ can generally be treated using the standard methods for localized states. This deep defect gives rise to some potential ΔV_+ that apart from a local part ΔV_{local} asymptotically approaches the potential of a screened point charge:

$$\Delta V_+(\mathbf{r}) = -\frac{e^2}{\epsilon_\infty r} + \Delta V_{\text{local}}(\mathbf{r}). \quad (17.36)$$

The extra electron e^- present in the neutral charge state D^0 is delocalized and moves within this potential, hardly disturbing the electron density of the deep state D^+ .

Thus, the electron density for the extra electron is expected to coincide with the magnetization density of the donor state. Within the EMA [4] the extra electron is described by a single-particle wave function $\Psi(\mathbf{r})$ which obeys the Schrödinger equation

$$\left(-\frac{\hbar^2}{2m_e}\nabla^2 + V_{\text{host}}(\mathbf{r}) + \Delta V_+(\mathbf{r}) - E\right)\Psi(\mathbf{r}) = 0. \quad (17.37)$$

We expand $\Psi(\mathbf{r})$ into a complete orthonormal set of Bloch functions $\varphi_{n,\mathbf{k}}(\mathbf{r}) = u_{n,\mathbf{k}}(\mathbf{r})e^{i\mathbf{k}\cdot\mathbf{r}}$ leading to

$$\Psi(\mathbf{r}) = \sum_{n,\mathbf{k}} f_{n,\mathbf{k}} \varphi_{n,\mathbf{k}}(\mathbf{r}). \quad (17.38)$$

Moreover, only states near the minimum of the conduction bands are assumed to contribute to the expansion Eq. (17.38). Hence, the Bloch states obey $u_{n,\mathbf{k}}(\mathbf{r}) \approx u_{n,\mathbf{k}_0}(\mathbf{r})$ and their energies can be expanded around this extremum. For the simplest case of a non-degenerate conduction band edge at the Γ point of the Brillouin zone, we assume

$$E_{c,\mathbf{k}} = E_{c,\mathbf{k}_0} + \frac{\hbar^2}{2m^*}(\mathbf{k} - \mathbf{k}_0)^2, \quad (17.39)$$

with an isotropic conduction band mass m^* .

This brings us to an equivalent problem for the hydrogenic envelope function $\tilde{\Phi}(\mathbf{r})$: the effective mass equation (EME) reads

$$\left(-\frac{\hbar^2}{2m^*}\nabla^2 + \Delta V_+(\mathbf{r}) - (E - E_{c,\mathbf{k}_0})\right)\tilde{\Phi}(\mathbf{r}) = 0, \quad (17.40)$$

with m^* absorbing the periodic part of the potential. To proceed further we specify the potential ΔV_+ . Far away from the impurity ΔV_+ is approximated by the potential of a point charge screened by the dielectric constant ϵ_∞ . Anticipating that most of the particle density is delocalized, we approximate ΔV_+ by its asymptotic form $-\frac{e^2}{\epsilon_\infty} \cdot \frac{1}{r}$ and neglect the specific local part of the potential completely.

With these approximations the eigenvalue problem (17.40) is identical to the elementary quantum mechanics textbook problem of the hydrogen atom. The solution for a particle of mass $m^* = \beta m_e$ moving in the screened Coulomb-potential can be written as

$$\begin{aligned} \tilde{\Phi}_{n,l,m}(\mathbf{r}) &= \left(\frac{\beta}{\epsilon_\infty}\right)^{3/2} \cdot R_{n,l}\left(\frac{\beta}{\epsilon_\infty}|\mathbf{r}|\right) \cdot Y_{l,m}\left(\frac{\mathbf{r}}{|\mathbf{r}|}\right), \\ E_{n,l=c,k_0} &= \frac{\beta}{\epsilon_\infty^2} \frac{\text{Ry}}{n^2}. \end{aligned} \quad (17.41)$$

With $\epsilon_\infty \sim 10$ and $m^* \sim 0.1m_e$ we obtain an effective Rydberg energy of $\text{Ry}^* = 10^{-3}\text{Ry}$ and an effective Bohr radius $r_B^* = 10^2 r_B$. All approximations made appear to be valid under these conditions, except for the central cell, which contains a very

small fraction of the extra electron density only. For the computation of hf interactions the hydrogenic envelope function $\tilde{\Phi}$ must be replaced by the true wave function Ψ .

In disagreement with the values of 53.73 meV, 45.53 meV, and 42.73 meV determined experimentally for As, P, and Sb in silicon [55], the best EMA predicts 31.27 meV for all the group V donors. This failure is of course a consequence of the neglect of the local part ΔV_{local} of the potential that would be necessary to distinct between different atomic species. A suitable central cell correction must be found to account for the so-called *chemical shift* within the binding energies.

17.4.2

Conduction Bands with Several Equivalent Minima

Besides the shallow electron centers in the silver halides AgCl and AgBr [56], we are not aware of experimental shf interaction data for shallow donors in a direct semiconductor with a conduction band minimum at the Γ point. EPR and ENDOR data are available for donors in the more conventional semiconductors Si and SiC. These have several equivalent conduction band minima far off the Γ point of the Brillouin zone. For silicon *e.g.*, the conduction band has six minima at $\mathbf{k}_0^{(1)} = 0.854 \frac{2\pi}{a} (1, 0, 0)$, along the so-called Δ axis near the boundary of the Brillouin zone. The solutions for the i different conduction band minima (the valleys) are degenerate. In order to construct realistic wave functions, symmetrical linear combinations of the single-valley wave functions from all equivalent valleys are required.

Whereas the single-valley solutions $\tilde{\Phi}_{1,0,0}^{(i)}(\mathbf{r})$ decay exponentially without nodes, the symmetrized wave function

$$\tilde{\Phi}_{1,0,0}^{(A_1)}(\mathbf{r}) = \sum_{i=1}^6 \frac{1}{\sqrt{6}} \tilde{\Phi}_{1,0,0}^{(i)}(\mathbf{r}), \quad (17.42)$$

describing the ground state and transforming according to the A_1 irreducible representation of the group T_d is oscillatory because of the $e^{i\mathbf{k}_0^{(i)} \cdot \mathbf{r}}$ factors in Eq. (17.38). Except at the donor site, the resulting magnetization density appears to be hardly related to the lattice structure (see right part of Figure 17.7). It shows an additional artificial mirror symmetry with respect to the horizontal (001) plane through the donor which is absent in the atomic positions. In addition, the first node of $\tilde{\Phi}_{1,0,0,A_1}(\mathbf{r})$ nearly coincides with the nn ligand nucleus and, therefore, the isotropic shf interaction with the ^{29}Si nn nuclei (which one would naively assume to be largest) virtually vanishes.

17.4.3

Empirical Pseudopotential Extensions to the EMA

There were several attempts to find a central cell potential correction. Baldereschi [57] has pointed out that intervalley potential matrix elements are of particular importance. These are screened by the dielectric function $\epsilon(\mathbf{q} = \mathbf{k}_0^{(i)} - \mathbf{k}_0^{(j)})$ rather than by the

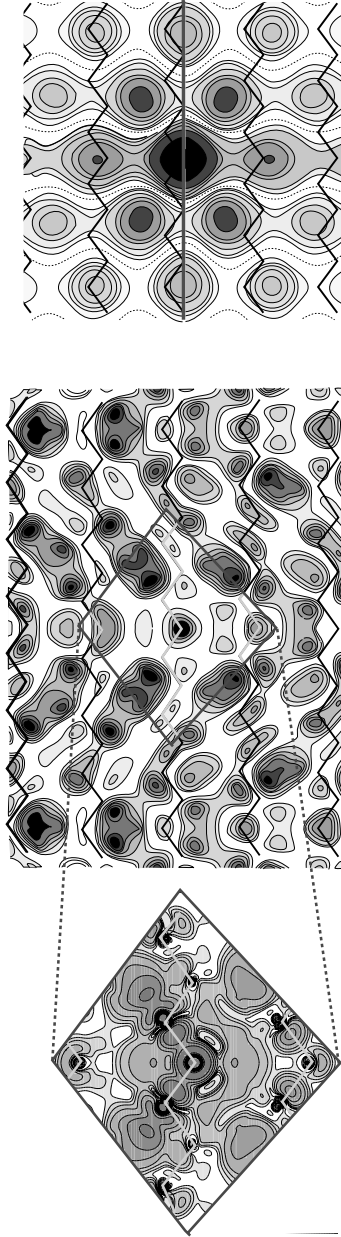


Figure 17.7 (online color at: www.pss-b.com) Contour plot of the electron density in the $(1\bar{1}0)$ plane for As_{Si}^0 in Si calculated via the LMTO-GF scheme (left part). Right: Contour plot of the impurity electron density in the $(1\bar{1}0)$ plane for a shallow donor in silicon according to the EMT of Hale and Miehler [64] (the donor atom is indicated by the black dot) and the same according to the empirical pseudopotential theory Ivey and Miehler [60] (central).

full dielectric constant ϵ_∞ . Several empirical pseudopotential schemes have been developed giving reliable ground state donor binding energies (for a review, see Pantelides [58]). Among these calculations, the calculation of Ivey and Miehler [59, 60] for group V donors in Si undertakes a calculation of the shf interactions. A model pseudopotential screened by the dielectric function is fitted to reproduce the experimental binding energy. In contrast to the EMA calculations, all \mathbf{k} points throughout the Brillouin zone are sampled and $u_{n,\mathbf{k}}(\mathbf{r})$ is not approximated by some $u_{n,\mathbf{k}_0}(\mathbf{r})$. If compared to the EMA density, the resulting density of the donor electron has lost the mirror symmetry, retaining only the desired A_1 symmetry of the atomic structure (see also central part of Figure 17.7). The shf interaction of the nearest neighbors, however, are still by about two orders of magnitude too small. In consequence of this failure of the EMA and its extensions, the wealth of information contained in the shf interaction data for shallow donors is completely obscured. In the best case we need an *ab initio* calculation to unravel the experimental data. Without such a calculation we cannot identify a single ligand shell from its shf interaction data.

17.4.4

Ab Initio Green's Function Approach to Shallow Donors

In section 17.3.3 we have shown, that the Green's function method allows an accurate description of the hf interaction, already if the perturbed region contains only 10% of the magnetic moment of a deep defect. It is this observation that brings us to the idea that the same should also be possible in the case of shallow states where up to 90% of the delocalized electron are found outside the largest conceivable perturbed region. Hence, the basic idea is now to substitute the empirical part of the EMA, the central cell correction, by a first-principle description in which ΔV_{local} in Eq. (17.36) is calculated self-consistently and embedded via a Green's function approach into an otherwise periodic, EMT-like background [61].

Similar to the case of the As-antisite in GaAs, we solve Dyson's equation within a "perturbed region" that contains the donor and five shells of ligands (47 atoms in total) and six shells with 42 "empty" spheres to reduce the overlap of the ASA spheres. In the ENDOR experiments for group-V donors in Si no symmetry-lowering lattice distortions have been detected [62]. Minimizing the LMTO-ASA total energy by a symmetry-conserving relaxation of the nearest neighbor distances we find a minimum for a nearest neighbor distance that is decreased by 1% for P_{Si}^0 , and increased by 3% As_{Si}^0 and by 6% for Sb_{Si}^0 , respectively with respect to the distance in a perfect Si crystal. For P_{Si}^0 and As_{Si}^0 , these values are reproduced by 216-atom supercell calculations [63]. For Sb_{Si}^0 , however, a considerably larger outward relaxation of 9% is predicted. We are of course more confident to the supercell geometry where all atoms are allowed to relax freely. Hence, in all what follows we use the 9% supercell-value for Sb_{Si}^0 . By this, we obtain considerably improved values if compared with the values given in our original work [61].

Since in our approach we ignore the long-range tail of the Coulomb-potential for that part of the induced density that is not contained within the perturbed region, we

do not find a shallow gap state but rather a resonance just above the onset of the conduction band. Thus, we cannot hope to obtain meaningful donor energies by this approach.

Figure 17.8 shows the change of the density of states (DOS) introduced by the defect (the “induced” DOS) for the three group-V donors in comparison with the DOS of the unperturbed crystal. In our approach we separate densities that arise from states transforming according to the different irreducible representation of the group T_d . In Figure 17.8 we display the a_1 -like densities only, suppressing the t_2 and e -like resonances that are ascribed to excited states. The induced DOS for P_{Si}^0 and As_{Si}^0 show a relatively well-defined minimum near 1.6 eV above the valence band edge, for Sb_{Si}^0 the resonance is much less pronounced. Starting from an effective one-particle picture, we shall consider the induced DOS below this minimum as a substitute for the shallow gap state. It contains about 15% of an electron within the perturbed region for P_{Si}^0 and As_{Si}^0 , while for Sb_{Si}^0 we find as little as 8% of an electron. Identifying the resonance below the minimum with the extra electron, we calculate the spin polarization of all electrons within the LSDA. The resulting magnetization density plotted for As_{Si}^0 in Figure 17.7 (left) is qualitatively different from the EMT result (right), in that it does not show the spurious inversion symmetry characteristic for the EMT. Instead it has some similarities with the envelope function obtained by Ivey and Mieher (central), with the clear distinction that there is no well-defined minimum at the nearest neighbors. A more detailed comparison of the different approaches is, however, possible via hf and shf data of ENDOR spectra, showing that our present approach is superior to the Ivey and Mieher (I-M) and the EMT methods (see Tables 17.2 and 17.3):

For the central donor nuclei the experimental values for the hf splitting are nicely reproduced within 5% for all donors – P, As, as well as Sb. Also for the nearest neighbor (1,1,1) shell, the isotropic and anisotropic shf interactions of our resonance

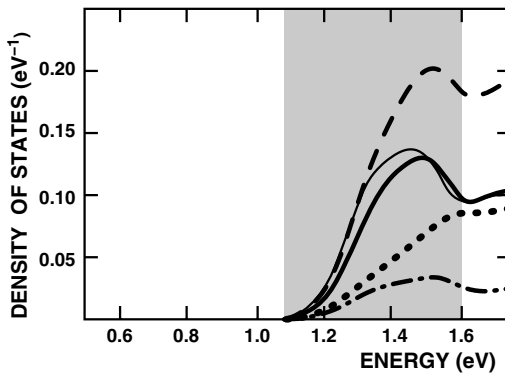


Figure 17.8 Density of states per impurity (DOS) that transform according the a_1 irreducible representation of the point group T_d for group-V donors in silicon. The (bold) full line denotes the induced density of the (un)relaxed

As_{Si}^0 , the dashed line is for P_{Si}^0 and the dash-dotted line is for the Sb_{Si}^0 donors. The dotted line represents the a_1 density of the unperturbed Si crystal. The grey area denotes the energy interval of the a_1 resonance.

Table 17.2 Isotropic hf and shf interactions (in MHz) for group-V donors in Si. Experimental values from Ref. [62] are compared with theoretical results of the present LMTO-GF approach, the pseudopotential approach from Ivey and Miehler (I-M), and an EMT approach. All data shown have a negative sign. For Sb the values in parenthesis belong to a smaller ligand relaxation (6% instead of 9%).

shell	donor	exp.	this work	I-M	EMT
(0,0,0)	³¹ P	117.5	121.4	71.2	448.
	⁷⁵ As	198.3	198.6	120.0	850.
	¹²¹ Sb	186.8	175.4 (66.8)	89.4	548.
(1,1,1)	P	0.540	0.518	0.036	1.524
	As	1.284	1.168	0.060	2.424
	Sb	0.586	0.405 (2.053)	0.090	1.232
(2,2,0)	P	–	0.115	0.608	0.861
		–	0.193	0.788	1.216
	Sb	–	0.312 (0.587)	0.532	0.734
(1,1, $\bar{3}$)	P	–	0.053	–	–
	As	–	0.179	–	–
	Sb	–	0.025 (0.001)	–	–
(0,0,4)	P	5.962	2.963	5.484	8.414
	As	7.720	3.160	7.606	11.400
	Sb	6.202	3.725 (2.923)	6.202	7.324
(3,3,1)	P	1.680	1.461	1.776	0.988
	As	2.242	2.351	2.590	1.290
	Sb	1.008	0.910 (0.848)	1.212	0.872

states compare favorably with the experimental data. The agreement is in fact much closer than for the I–M and EMT results for this shell. This becomes in particular clear if analyzing the ratio b/a which characterizes the hybridization at the (111) ligand shell (See also Table 17.3). For P and As, the values are rather insensitive to lattice relaxations. In case of Sb however, the 9% outward relaxation is necessary to predict a correct hybridization, $b/a = 1.09$ in comparison with the experimental ratio $(b/a)_{\text{exp}} = 0.89$. Note that for a reduced relaxation of 6% a much too small anisotropy ratio of 0.12 is obtained [61]. The next two neighbor shells have not been identified experimentally, presumably because the isotropic shf constant is below about 600 kHz, the “continuum” of many overlapping ENDOR lines. This explanation is in line with our results. Note that for the (2,2,0) shell both I–M and EMT predict hf interactions that in contrast should be readily observed. For the (0,0,4) shell the isotropic shf data are predicted too small by a factor of 2. For the outermost (3,3,1) shell in the perturbed region our results compare again quite well with the experimental data.

Table 17.3 Anisotropic hf and shf interactions (the axial component b in MHz) for group-V donors in Si. In contrast to the pseudopotential approach from Ivey and Mieher (I-M) [60], our LMTO-GF values compare reasonably well with the experimental hybridization ratio b/a [62]. For Sb the values in parenthesis belong to a smaller ligand relaxation (6% instead of 9%).

shell	donor	exp.		this work		I-M	
		b	b/a	b	b/a	b	b/a
(1,1,1)	P	0.70	1.296	0.66	1.274	0.49	13.611
	As	1.26	0.981	1.14	0.976	0.93	15.500
	Sb	0.52	0.887	0.44	1.086	0.35	3.844
(2,2,0)	P	—	—	(0.25)	(0.122)	0.03	0.049
	As	—	—	0.01	0.087	0.03	0.038
	Sb	—	—	0.02	0.104	0.02	0.038
(0,0,4)	P	0.02	0.003	(0.06)	(0.102)	0.02	0.004
	As	0.03	0.004	0.02	0.007	0.02	0.003
	Sb	0.02	0.003	0.02	0.006	0.02	0.003
(3,3,1)	P	0.06	0.036	(0.05)	(0.017)	0.04	0.023
	As	0.08	0.036	0.05	0.034	0.08	0.031
	Sb	0.03	0.030	0.09	0.038	0.03	0.025
				0.04	0.040		
				(0.03)	(0.035)		

Altogether, the oscillating behavior of the shf splitting is qualitatively correct described. In contrast, the one-particle theories are by no means able to describe the correct order of the contribution of the different shells. Ivey and Mieher [60] have suggested that the discrepancy in their pseudopotential approach is due to the neglect of the lattice relaxations, an explanation that at least for P and As is not supported by our results. More important, according our Green's function calculation, the shf interactions are only to a small part due to the conduction band resonance: more than 75% of the isotropic shf is caused by the spin polarization of the valence band states. Such polarizations are not included in the one-electron approach of I-M, which may explain in part the striking discrepancy between the experimental data and the results of the one-electron theories.

The agreement between theoretical and experimental hf and shf data, confirms that the resonance is a valid representative of the ground state of the shallow defect state. One may wonder whether these interferences can be found in an approach where the Coulomb-potential that extends outside of the perturbed region has to be cut. However, we have to note again that there is a clear distinction between the long-ranged *wave function* and the long-range part of the *Coulomb-tail of the potential*, although the two quantities are of course not completely independent. Whereas the latter determines predominantly the ionization levels, it is the spatial distribution of the wave function that gives rise to the shf splittings. It is the specific benefit of the Green's function approach that it allows to describe the wave function of a defect

correctly, although some parts of the long-ranged Coulomb-tail of the potential are ignored or approximated in a simple way. In order to prove that our shf results really do not suffer from termination errors we have calculated Green's functions for different perturbed regions. When decreasing the size of the perturbed region, the maximum of the resonance slightly shifts to higher energies, thereby decreasing the moduli of all hf and shf data monotonously. This decrease is not dramatic and amounts to less than 10% if we come down to a perturbed region that consists of the donor and 2 shells of ligands.

17.5

Phosphorus Donors in Highly Strained Silicon

Several approaches to build up solid-state based quantum computing hardware are actively pursued. The possible integration with existing microelectronics and the long decoherence times [65–67] are particular advantages if using the nuclear or electronic spins of phosphorus donors in group-IV semiconductors as qubits [68–71]. These concepts require gate-controlled exchange coupling between neighboring donors. However, to control the exchange coupling in semiconductors, the donor atoms have to be positioned with atomic precision [72] since the strength of the hf interaction, decisive for the rate at which two-qubit operations can be performed, varies strongly at the atomic scale due to Kohn–Luttinger oscillations of the donor wave function [69, 73, 74], already discussed in the last section. Under uniaxial compressive strain in [001]-direction, two conduction band minima are lowered in energy which is expected to suppress the oscillatory behavior in the (001) lattice plane [73].

In a recent work [75], the hf interaction of phosphorus donors in silicon was studied as a function of uniaxial compressive strain in thin layers of Si on virtual SiGe substrates, extending the regime investigated by Wilson and Feher [76] by a factor of 20 to higher strains. Fully strained 15 nm-thin P-doped ($[P] \simeq 1 \times 10^{17} \text{ cm}^{-3}$) silicon epilayers were grown lattice matched on virtual relaxed $\text{Si}_{1-x}\text{Ge}_x$ substrates with Ge-contents $x = 0.07, 0.15, 0.20, 0.25$, and 0.30 . The $\text{Si}_{1-x}\text{Ge}_x$ layer determines the strain of the Si epilayer: The higher lattice constant of SiGe alloys with respect to Si leads to biaxial tensile strain, accompanied by a compensating uniaxial compressive strain in growth direction (cf. inset in Figure 17.9), whereby the substrate with the highest Ge-content leads, of course, the largest strain. By high-resolution X-ray diffraction (XRD) it was shown that the compression in growth direction indeed follows linear elasticity theory.

To observe the P donors with high sensitivity, electrically detected magnetic resonance (EDMR) was used which monitors spin resonance via the influence of spin selection rules on charge transport processes [77–79]. The unstrained silicon layer provides the expected fingerprint of an isolated P-donor [80, 81] with an isotropic g -factor of $g = 1.9985$, whereby the characteristic hf-split satellite lines with a separation of $A_{\text{hf}} = 117.5 \text{ MHz}$ are clearly resolved. For the strained epilayers, in contrast, the hf splitting decreases monotonously with the applied strain. Simulta-

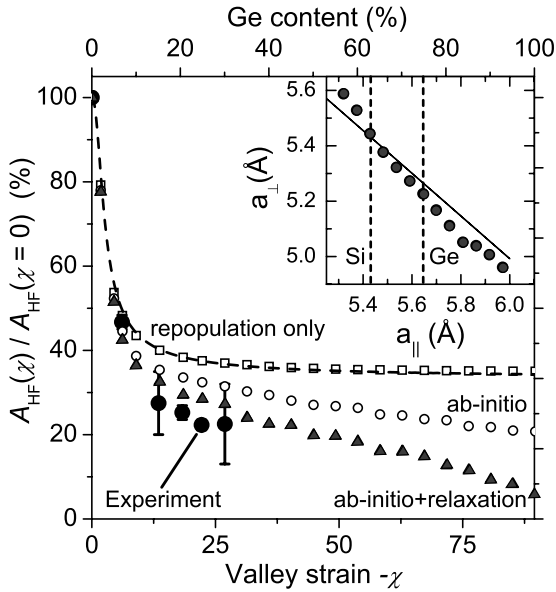


Figure 17.9 (online color at: www.pss-b.com) Relative hf splittings observed for P in fully strained epilayers on $\text{Si}_{1-x}\text{Ge}_x$ substrates as a function of the Ge content x and the resulting valley strain $\chi = \sim (a_{\parallel} - a_{\perp})$ (see also Ref. [75]). Black dots indicate the experimental data. The DFT-results for valley repopulation only are indicated by open squares and reproduce the prediction of Wilson and Feher (dashed line). The influence of strain-induced volume change

is shown by open circles, whereby those additionally including nn relaxation are shown by triangles. The insert shows the out-of-plane lattice constant a_{\perp} of thin Si layers (thickness 12 unit cells) as a function of the in-plane constant a_{\parallel} predicted by supercell calculations compared to linear elasticity theory (straight line). Pure Si and Ge substrates are shown by dashed vertical lines.

neously, the resonance line becomes clearly anisotropic. For example, for the epilayer with $(a_{\perp} - a_{\text{Si}})/a_{\text{Si}} = -0.00729$ obtained by a substrate with 25% Ge content, the isotropic hf splitting shrinks to 26.9 MHz, while $\Delta g = (1.21 \pm 0.06) \times 10^{-3}$.

17.5.1

Predictions of EMA

For an isolated P donor atom in unstrained Si, the isotropic Fermi-contact hf interaction A_{hf} in the non-relativistic limit is proportional to the probability amplitude $|\psi(0)|^2$ of the unpaired electron wave function at the nucleus, giving rise to the hf satellite lines separated by $A_{\text{hf}} = 117.5$ MHz. To determine $|\psi(0)|^2$, we first note that the cubic crystal field leads to the formation of a singlet ground state and a doublet and a triplet of excited states instead of a six-fold degenerate ground state. Only the fully symmetric singlet ground state has a non-vanishing probability amplitude at the nucleus.

In Section 17.4.2 we have seen that the A_1 ground state wave function ψ is given by the symmetrical superposition $\psi(\mathbf{r}) = \sum_{i=1}^6 (1/\sqrt{6}) \Phi^{(i)}(\mathbf{r})$ of the six valleys contributing to the donor, whereby each $\Phi^{(i)}$ is a product of the corresponding conduction band Bloch wave function and a hydrogenic envelope function. The probability of the unpaired electron at the nucleus $|\psi(0)|^2$ becomes $1/6 |\sum_{j=1}^6 \Phi^{(j)}(0)|^2 = 6|\Phi(0)|^2$, since due to degeneracy $\Phi^{(i)}(0) = \Phi(0)$ for all i . Assuming that the only effect of strain is the change of relative population of the conduction band minima, we similarly find $\psi = \sum_{i=1}^2 (1/\sqrt{2}) \Phi_i$ and $|\psi(0)|^2 = 2|\Phi(0)|^2$ under high uniaxial strain, when only two conduction band minima contribute. Therefore, in the fully strained case, the hf interaction should be 1/3 of the unstrained case.

In contrast, in Figure 17.9 we already observe a reduction to 0.21 of the unstrained hf interaction A_{HF} , clearly below the 0.33 A_{HF} EMA-limit obtained above. Based on group and linear elasticity theory Wilson and Feher [76] evaluated the analytical dependence of $A_{\text{hf}}(\chi)$ from the so-called valley strain $\chi = -\frac{\Xi_u}{3\Delta_c} (a_{\parallel} - a_{\perp})$, where $\Xi_u = 8.6$ eV is the uniaxial deformation potential [82], and $6\Delta_c = 2.16$ meV [54] is the energy splitting between the singlet and doublet state in the unstrained material. In Figure 17.9, a comparison of the prediction of Eq. (17.2) in Ref. [76] (dashed line) with the hf splittings determined experimentally (full circles) clearly shows, that pure valley repopulation is not able to describe the experimental data for $\chi > 0.07$. An empirical treatment of additional radial redistribution effects as discussed in Ref. [83] would lead to 0.29 for $\chi \rightarrow -\infty$, only a slight reduction of the repopulation-limit and, thus, still at strong variance with the experimental data.

17.5.2

Ab Initio Treatment via Green's Functions

Again, an *ab initio* prediction of hf interactions is necessary to clarify the situation. In the last section, our Green's function approach has been shown to describe the hf splittings in predictive accuracy for P_{si} in the unstrained case. In the case of a strained host material, however, the situation becomes more complicated since excited states are admixed to the former pure singlet ground state. An application of DFT is, thus, only possible in combination with linear elasticity theory: Due to the applied strain, the symmetry of the P donor is reduced, and the resonance at the bottom of the CB transforming according the a_1 representation in the unstrained case, now shows admixtures of the b_1 and b_2 representations of D_{2d} symmetry (cf. Figure 17.10). The location of the P donor atom in their nodal planes implies a correlation of these b_1 and b_2 -like orbitals with the admixed doublet state. Since, furthermore, only one component of the diamagnetic doublet state is contributing to the singlet ground state under strain [76], it is reasonable to construct the spin densities, which enter the self-consistent LSDA total energy calculations for a given valley strain, by $n^{\sigma}(r) = (1 - \alpha(\chi)) \cdot n_{a_1}^{\sigma}(r) + \alpha(\chi) \cdot n_{b_1}^{\sigma}(r)$, whereby $\alpha(\chi)$ is obtained from the strain-dependent admixture of the doublet states determined by linear elasticity theory (see Eq. (C6) in Ref. [76]). Figure 17.9 shows that the spin densities constructed this way allow a reasonable description of the pure valley repopulation effect: for an *unrelaxed*

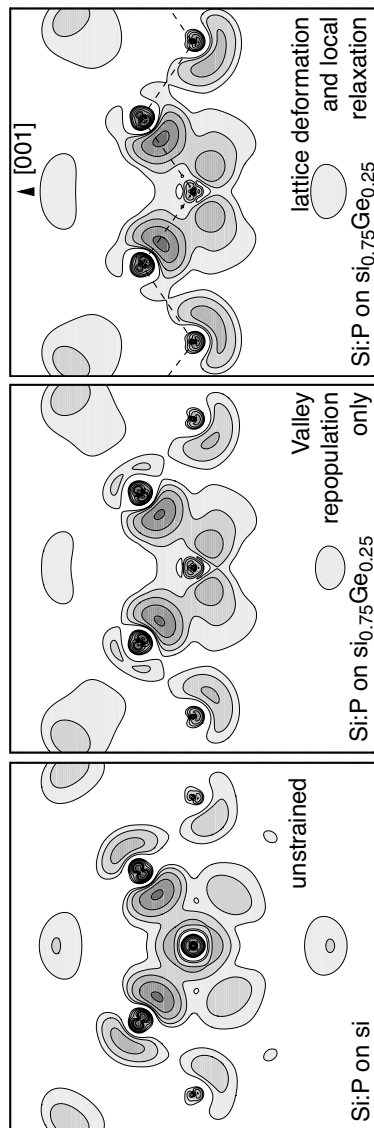


Figure 17.10 (online color at: www.pss-b.com) Plot of the magnetization density in the (110) plane around the P donor atom in unstrained silicon (left) and in material strained by a Si_{0.75}Ge_{0.25} substrate determined by valley repopulation (central) and including the change in the volume and local relaxation of the donor (right).

structure of an *ideal* silicon crystal, the results obtained by Wilson and Feher [76] are nicely reproduced after the self-consistent cycle (cf. open squares in Figure 17.9).

We are now able to take into account explicitly by *first principles* the strain of the silicon lattice as well as the relaxation around the P donors within. For the optimization of the strained Si cells, we used a supercell approach [84]. Optimization of long slabs (up to 12 unit cells along the (001)-direction) show an almost linear dependence of the compression along (001) as an answer to the tensile strain in the (001)-plane, effectively following linear elasticity theory as indicated in the inset of Figure 17.9. This result confirms that *linear* elasticity theory remains valid in the complete regime, even up to pure germanium as a substrate ($\chi \approx -89$). The hf parameters calculated with LMTO-GF under these assumptions (cf. open circles in Figure 17.9) already become smaller since the donor wave function becomes more delocalized as a result of the enhanced volume, lifting the high-stress limit of $0.33A_{\text{HF}}$ obtained above. This tendency is strengthened, if local relaxation around the P donors is taken into account: According to total energy calculations on large explicitly strained supercells with 512 atoms, this relaxation is dominated by a slight reduction of the bond-length between the P donor and its nearest Si ligands by about 1%, nearly independent of the strength of the tensile strain in the plane of the Si epilayer. Recalculating $A_{\text{hf}}(\chi)/A_{\text{hf}}(0)$ for this geometry with the LMTO-GF code, we find a further reduction (open triangles in Figure 17.9). In addition, being *e.g.*, in the unstrained case about 50 MHz too large before, also the absolute values A_{hf} are then in nice accordance with experiment. The hf interaction observed experimentally in the moderately strained P-doped silicon layers can, thus, be explained by the increased volume of the unit cell together with a slight inward relaxation of the nearest Si neighbors. Since already such a small relaxation has a huge influence on the predicted relative hf splittings for the strained material, the remaining discrepancy between experiment and theory can easily be explained by uncertainties due to the well-known flatness of the total energy surface in silicon [85]. Apparently, there exists no high-stress limit for the reduction of the P-related hf splitting. According to our DFT calculation the decrease of the central P-related hf interaction is accompanied by a remarkable increase of the shf interaction with neighboring ^{29}Si atoms.

17.6

n-Type Doping of SiC with Phosphorus

For high temperature and high frequency applications, silicon carbide (SiC) has been proven to provide in principle many advantages over silicon or gallium arsenide [86]. However, its technology, *e.g.* *n*-type doping, is considerably more difficult than that of silicon: although nitrogen is easily incorporated during growth, the electrical conductivity saturates at higher doping concentrations [87, 88]. The alternative shallow donor, phosphorus, cannot be easily introduced into the material by diffusion. One must fall back on other doping techniques like ion implantation, *in situ* doping during growth or neutron transmutation of ^{30}Si [89].

From the transmutation process $^{30}_{14}\text{Si} \xrightarrow{(n,\gamma)} ^{31}_{14}\text{Si}^* \xrightarrow{\beta} ^{31}_{15}\text{P}$ it was assumed for long time that the so created P-dopants enter the silicon sublattice. At first view, this assumption is also supported by total energy calculations: the formation energy of P_{Si} is essentially lower (by 1.5 eV) than for P incorporated at the carbon sublattice. However, the large number of different spectra observed in electron paramagnetic resonance (EPR) [90–94], at least six, can by no means be explained by one single defect at different lattice sites. Indeed, molecular dynamic (MD) simulations including the recoil process and the following annealing processes result in various P-related defects [95]. Due to kinetic effects during the recoil (770 eV after capture of thermal neutrons [96]) and subsequent annealing processes, an incorporation of P at the carbon sublattice becomes possible. The inconsistencies in early models for the P-related donors in SiC are a consequence of neglecting this possibility. Beside the already discussed donors (P_{Si} , P_{C} , $\text{P}_{\text{Si}}\text{V}_{\text{C}}$ [97]) alternative complexes with intrinsic defects (e.g. $\text{P}_{\text{C}}\text{C}_{\text{Si}}$) are predicted with high probability [95]. At usual annealing temperatures, the exchange mechanism toward isolated P_{Si} is hindered. Although providing much lower formation energy, due to a large activation barrier of about 5 eV, extremely high temperature annealing above 2000 K is expected to be necessary to achieve a reasonable incorporation of P at the Si-sublattice, and allows the observation of P_{C} in moderately annealed samples.

This scenario is supported by our *ab initio calculation* of the corresponding hf splittings. Like isolated P at the silicon site, P_{C} and $\text{P}_{\text{C}}\text{C}_{\text{Si}}$ are calculated to act as shallow donors. Thus, we use again the EMT embedded Green's function method to model the shallow defect states. As a first reference in the compound semi-conductor SiC, we applied our extended method to the well-known nitrogen donors N_{C} in 6H-SiC. As can be seen in Table 17.4, the experimental values are well reproduced: at the hexagonal site (h) minor additional relaxation occurs compared to the ionized donor N_{C}^+ retaining a tetrahedral arrangement of the ligands (slightly outward relaxed by about 5% of the bond-length). A rather small hf splitting below 5 MHz is the consequence. For the quasi-cubic sites (k_1 , k_2) in contrast, a small distortion toward C_{3v} -symmetry (one ligand relaxes 7% away from the donor atom) yields an increased

Table 17.4 Calculated and observed hf parameters (MHz) for P-related EPR-spectra in 6H-SiC (see Ref. [94] for a review). Note that for the quasicubic sites (k_1 , k_2) only minor differences in the calculated values (below 0.4 MHz) can be observed. Here, only the values for the k_2 -site are given.

defect	site	a_{calc}	b_{calc}	center	a_{exp}	b_{exp}
N_{C}	h	4.49	0.00	N_{h}	2.47	0.13
N_{C}	k_1, k_2	28.48	1.05	N_{k_1, k_2}	33.40	0.01
P_{Si}	h	1.76	0.59	I_1	1.56	0.89
P_{Si}	k_1, k_2	8.75	2.78	I_2	8.70	4.20
P_{C}	h	156.1	0.00	P_1	145.0	0.00
P_{C}	k_1, k_2	147.2	5.04	$\text{P}_2?$	156.0	0.70
$\text{P}_{\text{C}}\text{C}_{\text{Si}}$		169.8	−0.10			
$\text{P}_{\text{Si}}\text{V}_{\text{C}}$		−20.6	3.54	$\text{P} + \text{V}$	22.0	1.87

hf splitting of 28.5 MHz (exp. 33.4 MHz). Note that the observation that more pronounced distortions occur at the quasi-cubic sites whereas the hexagonal sites mimic the lattice sites in the cubic material is also reported in case of the carbon vacancy in 4H-SiC [98, 99].

We obtain the same trend when applying the Green's function-based method to the isolated P-donors at the silicon sublattice (P_{Si}). However, compared to the P_1 , P_2 spectra (originally assigned to P_{Si}), the values are by about a factor of 20 too small. The calculated values fit, instead, very well to the second set of spectra (I_1 , I_2 , see also Table 17.4 and the upper part of Figure 17.11). Large, rather isotropic hf splittings in the range of 150 MHz can only be obtained for P at a carbon site – an observation which is in line with the results of our MD calculations. The isotropic spectrum P_1 is most likely due to P_C at the hexagonal site (again retaining essentially a tetrahedral arrangement of the ligands but with a more pronounced outward relaxation of about 15%) whereas an explanation of the P_2 spectra with a small but non-vanishing anisotropic part requires C_{3v} -symmetry, either obtained by a distortion around the quasi-cubic sites or by a nearby carbon antisite (Figure 17.11). We no longer expect that the P_1 , P_2 and $P + V$ lines are caused by one center at three different lattice sites as argued in the more recent models [92, 93]. In this point, based on the calculated hf parameters, we come back to the original model of Veinger *et al.* [90], instead, and reassign the so-called $P + V$ center to a $P_{Si}V_C$ pair (Table 17.4).

Further confirmations of our model have been later obtained from additional EPR measurements on the 3C-SiC and 6H-SiC polytypes [53] as well as from investigations on different new 4H-SiC samples: (1) the first was doped *in situ* with phosphorus grown by the PVT method using SiP_2O_7 as a source [89]; (2) the second, based on our theoretical results, have been ^{30}Si -enriched (50% instead of about 3% natural abundance) in order to reexamine neutron transmutation. In one point, both samples show a similar result: intense lines of the $P + V$ center can be resolved, but even no trace of the P_1 and P_2 spectra. Hence, one has clearly to rule out any model in which P_1/P_2 differ from the $P + V$ center by the lattice site only. The absence of the P_C -related spectra can be explained by high temperature annealing (sample 2) and by an incorporation of the P-donors close to the thermal equilibrium during growth (sample 1). However, only in the ^{30}Si -enriched, the I_1/I_2 spectra of P_{Si} can be easily resolved in comparable intensity, whereby in the sample *in situ* doped during growth the lines are expected being covered by the intense central resonance line of the N-donor.

17.7

Conclusions

We have shown that a Green's functions approach is able to calculate hf splittings of shallow donors in semiconductors in predictive accuracy, whereby the *ab initio* calculated local part of the potential, the central cell correction of effective mass theory (EMT), is embedded via Green's functions into a periodic, EMT-like background. The method was successfully applied onto shallow donors in Si and SiC: hf parameters of donors in silicon (P, As, Sb) are reproduced in quantitative agreement with exper-

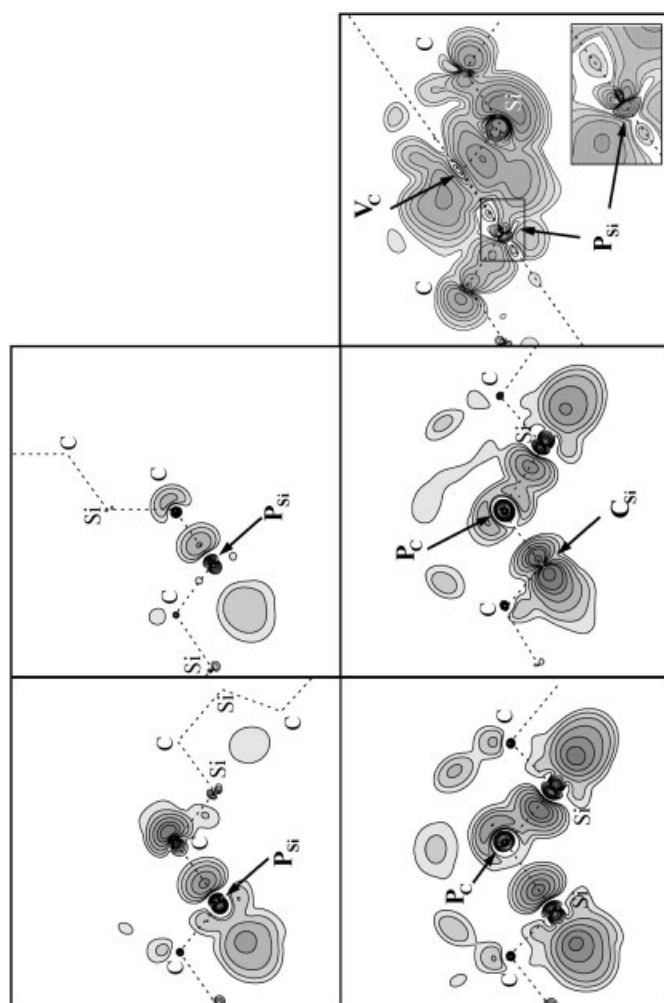


Figure 17.11 (online color at: www.pss-b.com) Magnetization density of some P-related donor states in 6H-SiC in a (110)-plane: In case of P on the silicon sublattice (top: P_{Si} at a quasi-cubic site k_z (left part) and at the hexagonal site h (right)), p -like spin densities at the donor nucleus occur, explaining the small, mainly anisotropic hf splittings of the $I_{1/2}$ spectra. In contrast, P_C and $P_C Si$ (bottom) provide s -like spin densities around the ^{31}P nuclei and, thus, rather isotropic hf parameters (Table 17.4). For comparison, the corresponding plot for the $P_C C_{Si}$ deep defect pair is also given (bottom right).

imental data including the so-called Kohn–Luttinger oscillations due to the neighbor shells. For P in strained silicon, a relaxation of the next nearest (nn) silicon neighbors is shown to be crucial to explain quantitatively the experimentally observed decrease of hf interaction, whereby our results indicate that in contrast to the prediction of the EMA, there exists no high-stress limit for the reduction of the P-related hf splitting. It is also confirmed that by strain the Kohn–Luttinger oscillations can be partially suppressed. Both observations are crucial for quantum computing applications since the spatial distribution of the hf interaction has a direct impact on the rate with which two-qubit operations can be performed. The application of the approach onto N and P donors in SiC confirms an incorporation of the P atoms onto both, the silicon as well as the carbon sublattice.

It is now possible to treat shallow donors without invoking a one-electron approximation and several fitting parameters. The presented *ab initio* calculations, although considerably more complex, are much more flexible and furthermore their application requires considerably less manpower than one of the usual, more involved one-electron EMA methods for shallow defects. Most probably our method cannot be extended directly to supercells containing a few hundred atoms, because here the periodic images of the defect superlattice are still superimposed into each cell. But it is not unlikely that for cluster calculations a similar extension will hold, whereby in principle the unperturbed Green's function can be obtained from a supercell calculation of the corresponding ionized donor. This would be very promising, since in a Green's function approach the *ab initio* calculation results in hf and shf interactions that for the center region of the defect are considerably more accurate than those obtained from the best empirical approaches.

Acknowledgements

This work is dedicated to Harald Overhof. Furthermore, I am grateful to all my collaborators, theoreticians as well as experimentalists, who made the scientific work and this article possible. The work was partially supported by the Deutsche Forschungsgemeinschaft (DFG).

References

- 1 Kohn, W. (1999) *Rev. Mod. Phys.*, **71**, 1253.
- 2 Kohn, W. and Luttinger, J.M. (1955) *Phys. Rev.* **97**, 1721. *Phys. Rev.*, **98**, 915 (1955).
- 3 Luttinger, J.M. and Kohn, W. (1955) *Phys. Rev.*, **97**, 969.
- 4 Kohn, W. (1960) Shallow impurity states in silicon and germanium, in: *Solid State Physics* 5, eds F. Seitz and D. Turnbull Academic Press, New York, p. 1.
- 5 Hohenberg, P. and Kohn, W. (1964) *Phys. Rev. B*, **136**, 864.
- 6 von Barth, U., and Hedin, L. (1972) *J. Phys. C* **5**, 1629.
- 7 Kohn, W. and Sham, L.J. (1965) *Phys. Rev.*, **140**, A1133.
- 8 Ceperley, D.M. and Alder, B.J. (1980) *Phys. Rev. Lett.*, **45**, 566.
- 9 Perdew, P. and Zunger, A. (1981) *Phys. Rev. B*, **23**, 5048.

- 10 Perdew, J.P. and Levy, M. (1983) *Phys. Rev. Lett.*, **51**, 1884.
- 11 Sham, L.J. and Schlüter, M. (1983) *Phys. Rev. Lett.*, **51**, 1888.
- 12 Sanna, S., Frauenheim, Th., Gerstmann, U., and (2008) *Phys. Rev. B*, **78**, 085201.
- 13 Fermi, E. (1930) *Z. Phys.*, **60**, 320.
- 14 Breit, G. (1930) *Phys. Rev.*, **35**, 1447.
- 15 Blügel, S., Akai, H., Zeller, R., and Dederichs, P.H. (1987) *Phys. Rev. B*, **35**, 3271.
- 16 Bethe, H.A. and Negele, J.W. (1968) *Nucl. Phys. A* **117**, 575.
- 17 Abragam, A. and Bleaney, B. (1970) *Electron Paramagnetic Resonance of Transition Ions* (Clarendon Press, Oxford, (reprint: Dover Publications, New York, 1986).
- 18 Koster, G.F. and Slater, J.C. (1954) *Phys. Rev.*, **96**, 1208.
- 19 Baraff, G.A. and Schlüter, M. (1978) *Phys. Rev. Lett.*, **41**, 892; (1979) *Phys. Rev. B*, **19**, 4965.
- 20 Gunnarsson, O., Jepsen, O., and Andersen, O.K. (1983) *Phys. Rev. B*, **27**, 7144.
- 21 Economou, E.N. 1979 *Green's Functions in Quantum Physics* (Springer-Verlag, Heidelberg, New York).
- 22 Ferry, D.K. 2009 *Transport in Nanostructures* (Cambridge University Press, Cambridge, New York).
- 23 Spaeth, J.-M. and Overhof, H., 2003 *Point Defects in Semiconductors and Insulators, Springer Series in Material Science*, Vol. **53** (Springer Verlag, Heidelberg).
- 24 Baraff, G. and Schlüter, M. (1984) *Phys. Rev. B*, **30**, 3460.
- 25 Van de Walle, C.G., and Blöchl, P.E. (1993) *Phys. Rev. B*, **47**, 4244.
- 26 Korringa, J. (1947) *Physica* **13**, 392.
- 27 Kohn, W. and Rostoker, N. (1954) *Phys. Rev.*, **94**, 1111.
- 28 Andersen, O.K. (1975) *Phys. Rev. B*, **12**, 3060.
- 29 Skriver, H.L. 1984 *The LMTO method, Springer Series in Solid-State Sciences*, Vol. **41** (Springer Verlag Berlin, Heidelberg, New York).
- 30 Slater, J.C. (1937) *Phys. Rev.*, **51**, 846.
- 31 Drittler, B., Weinert, M., Zeller, R., and Dederichs, P.H. (1989) *Phys. Rev. B*, **39**, 930.
- 32 Methfessel, M., Rodriguez, C.O., and Andersen, O.K. (2009) *Phys. Rev. B*, **40**, 1989.
- 33 Blaha, P., Schwarz, K., Sorantin, P., and Trickey, S.B. (1990) *Comput. Phys. Commun.* **59**, 399.
- 34 Voronoi, G. (1908) *Crelle J.* **134**, 198.
- 35 Becke, A.D. (1988) *J. Chem. Phys.*, **88**, 2547.
- 36 Ohno, K., Esfarjani, K., and Kawazoe, Y. 1999 *Computational Materials Science* (Springer, Berlin, Heidelberg).
- 37 Krambrock, K. and Spaeth, J.-M. (1992) *Mater. Sci. Forum* **83/87**, 887.
- 38 Krambrock, K., Spaeth, J.-M., Delerue, C., Allan, G., and Lannoo, M. (1992) *Phys. Rev. B*, **45**, R1481.
- 39 Koschnick, F.K. and Spaeth, J.-M. (1999) *Phys. Status Solidi B*, **216**, 817.
- 40 Spaeth, J.-M. and Krambrock, K. 1994 in: *Festkörperprobleme/Advances in Solid State Physics*, Vol. 33, eds R. Helbig (Vieweg, Braunschweig), p. 111.
- 41 Holmes, D.E., Chen, R.T., Elliott, K.R., and Kirkpatrick, C.G. (1982) *Appl. Phys. Lett.*, **40**, 46.
- 42 Nissen, M.K., Villemaire, A., and Thewalt M. L. W. (1991) *Phys. Rev. Lett.*, **67**, 112.
- 43 Lagowski, J., Gatos, H.C., Kang, C.H., Skoronski, M., Ko, K.K., and Lin, D.G. (1986) *Appl. Phys. Lett.*, **49**, 892.
- 44 Overhof, H. and Spaeth, J.-M. (2005) *Phys. Rev. B*, **72**, 115202.
- 45 Dabrowski, J. and Scheffler, M. (1988) *Phys. Rev. Lett.*, **60**, 2183 ; *Phys. Rev. B*, **40**, 10391 (1989).
- 46 Chadi, D.J. and Chang, K.J. (1988) *Phys. Rev. Lett.*, **60**, 2187; (1988) *Phys. Rev. B*, **39**, 10 063.
- 47 Chadi, D.J. (2003) *Phys. Rev. B*, **68**, 193204.
- 48 Baraff, G.A. and Schlüter, M. (1985) *Phys. Rev. Lett.*, **55**, 2340.
- 49 Delerue, C. (1991) *Phys. Rev. B*, **44**, 10525.
- 50 Gerstmann, U. and Overhof, H. (2001) *Physica B*, **308–310**, 561.
- 51 Tkach, I., Krambrock, K., and Overhof, H., Spaeth, J.-M. (2003) *Physica B*, **340–342**, 353.
- 52 Duijn-Arnold, A.V., Zondervan, R., Schmidt, J., Baranov, P.G., and Mokhov, E.N. (2001) *Phys. Rev. B*, **64**, 085206.
- 53 Son, N.T., Henry, A., Isoya, J., Katagiri, M., Umeda, T., Gali, A., and Janzén, E. (2006) *Phys. Rev. B*, **73**, 075201.

- 54 Ramdas, A.K. and Rodriguez, S. (1981) *Rep. Prog. Phys.*, **44**, 1297.
- 55 Aggarwal, R.L. and Ramdas, A.K. (1965) *Phys. Rev.*, **140**, A1246.
- 56 Overhof, H. and Gerstmann, U. (2000) *Phys. Rev. B*, **62**, 12585.
- 57 Baldereschi, A. (1970) *Phys. Rev. B*, **1**, 4673.
- 58 Pantelides, S.T. (1978) *Rev. Mod. Phys.*, **50**, 797.
- 59 Ivey, J.L. and Miehler, R.L. (1972) *Phys. Rev. Lett.*, **29**, 176.
- 60 Ivey, J.L. and Miehler, R.L. (1975) *Phys. Rev. B*, **11**, 822; (1975) *Phys. Rev. B*, **11**, 849.
- 61 Overhof, H. and Gerstmann, U. (2004) *Phys. Rev. Lett.*, **92**, 087602.
- 62 Feher, G. (1959) *Phys. Rev.*, **114**, 1219.
- 63 Rockett, A., Johnson, D.D., Khare, S.V., and Tuttle, B.R. (2003) *Phys. Rev. B*, **68**, 233208.
- 64 Hale, E.B. and Miehler, R.L. (1971) *Phys. Rev. B*, **3**, 1955.
- 65 Castner, T.G., Jr (1962) *Phys. Rev. Lett.*, **8**, 13.
- 66 Tyryshkin, A.M., Lyon, S.A., Astashkin, A.V., and Raitsimring, A.M. (2003) *Phys. Rev. B*, **68**, 193207.
- 67 Gordon, J.P. and Bowers, K.D. (1958) *Phys. Rev. Lett.*, **1**, 268.
- 68 Kane, B.E. (1998) *Nature* **393**, 133.
- 69 Kane, B.E. (2000) *Fortschr. Phys.*, **48**, 1023.
- 70 Vrijen, R., Yablonovitch, E., Wang, K., Jiang H.W., Balandin, A., Roychowdhury, V., Mor, T., and DiVincenzo, D. (2000) *Phys. Rev. A* **62**, 012306.
- 71 Hollenberg, L. C. L., Dzurak, A.S., Wellard C., Hamilton, A.R., Reilly, D.J., Milburn, G.J., and Clark, R.G. (2004) *Phys. Rev. B*, **69**, 113301.
- 72 Schofield, S.R., Curson, N.J., Simmons, M.Y., Rueß, F.J., Hallam, T., Oberbeck, L., and Clark, R.G. (2003) *Phys. Rev. Lett.*, **91**, 136104.
- 73 Koiller, B., Hu, X., and Das Sarma, S. (2002) *Phys. Rev. B*, **66**, 115201.
- 74 Wellard, C.J., Hollenberg, L. C. L., Parisoli, F., Kettle, L.M., Goan, H.-S., McIntosh, J. A. L., and Jamieson, D.N. (2003) *Phys. Rev. B*, **68**, 195209.
- 75 Huebl, H., Stegner, A.R., Stutzmann, M., Brandt, M., Vogg, G., Bensch, F., Rauls, E., and Gerstmann, U. (2006) *Phys. Rev. Lett.*, **97**, 166402.
- 76 Wilson, D.K. and Feher, G. (1961) *Phys. Rev.*, **124**, 1068.
- 77 Schmidt, J. and Solomon, I. (1966) *Compt. Rend.* **263**, 169.
- 78 Stich, B., Greulich-Weber, S., and Spaeth, J.-M. (1996) *Appl. Phys. Lett.*, **68**, 1102.
- 79 Brandt, M.S., Goennenwein, S. T. B., Graf, T., Huebl, H., Lauterbach, S., and Stutzmann, M. (2004) *Phys. Status Solidi C* **1**, 2056.
- 80 Young, C.F., Poindexter, E.H., Gerardi, G.J., Warren, W.L., and Keeble, D.J. (1997) *Phys. Rev. B*, **55**, 16245.
- 81 Cullis, P.R. and Marko, J.R. (1975) *Phys. Rev. B*, **11**, 4184.
- 82 Tekippe, V.J., Chandrasekhar, H.R., Fisher, P., and Ramdas, A.K. (1972) *Phys. Rev. B*, **6**, 2348.
- 83 Fritzsche, H. (1962) *Phys. Rev.*, **125**, 1560.
- 84 Frauenheim, Th., Seifert, G., Elstner, M., Hajnal, Z., Jungnickel, G., Porezag, D., Suhai, S., and Scholz, R. (2000) *Phys. Status Solidi B*, **217**, 41.
- 85 Gerstmann, U., Rauls, E., Overhof, H., and Frauenheim, Th. (2002) *Phys. Rev. B*, **65**, 195201.
- 86 Choyke, W.J., Matsunami, H., and Pensl, G. eds, (2004) *Recent Major Advances in SiC* (Springer-Verlag, Berlin)
- 87 Pensl, G., Frank, T., Krieger, M., Laube, M., Reshanov, S., Schmid, F., and Weidner, M. (2003) *Physica B*, **340–342**, 121.
- 88 Gerstmann, U., Rauls, E., Frauenheim, Th., and Overhof, H. (2003) *Phys. Rev. B*, **67**, 205202.
- 89 Semmelroth, K., Schmid, F., Karg, D., Pensl, G., Maier, M., Greulich-Weber, S., and Spaeth, J.-M. (2003) *Mater. Sci. Forum* **433–436**, 63.
- 90 Veinger, A.I., Zabrodskii, A.G., Lomakina, G.A., and Mokhov, E.N. (1986) *Sov. Phys. Solid State* **28**, 917.
- 91 Kalabukhova, E.N., Lukin, S.N., and Mokhov, E.N. (1993) *Sov. Phys. Solid State* **35**, 361.
- 92 Greulich-Weber, S. (1997) *Phys. Status Solidi A* **162**, 95.

- 93 Baranov, P.G., Il'in, I.V., Mokhov, E.N., von Bardeleben, H.J., and Cantin, J.L. (2002) *Phys. Rev. B*, **66**, 165206.
- 94 Pinheiro, M. V. B., Greulich-Weber, S., and Spaeth, J.-M. (2003) *Physica B*, **340–342**, 146.
- 95 Rauls, E., Pinheiro, M. V. B., Greulich-Weber, S., and Gerstmann, U. (2004) *Phys. Rev. B*, **70**, 085202.
- 96 Heißenstein, H. (2002) Dissertation, Universität Erlangen, Germany.
- 97 Gali, A., Deák, P., Briddon, P.R., Devaty, R.P., and Choyke, W.J. (2000) *Phys. Rev. B*, **61**, 12602.
- 98 Bockstedte, M., Heid, M., and Pankratov, O. (2003) *Phys. Rev. B*, **67**, 193102.
- 99 Umeda, T., Isoya, J., Morishita, N., Ohshima, T., and Kamiya, T. (2004) *Phys. Rev. B*, **69**, 121201(R).